# Improvements to the parameterization of snow in AROME in the context of ice crystal icing

Jean Wurtz, Dominique Bouniol, Benoît Vié

Quarterly Journal of the Royal Meteorological Society
A journal of the atmospheric sciences and physical oceanography
RMetS

# Improvements to the parameterization of snow in AROME in the context of ice crystal icing

| | |
|---|---|
| Journal: | *QJRMS* |
| Manuscript ID | QJ-22-0030.R1 |
| Wiley - Manuscript type: | Research Article |
| Date Submitted by the Author: | 19-Nov-2022 |
| Complete List of Authors: | Wurtz, Jean; Meteo-France CNRM/GMME/TROPICS,<br>Vié, Benoît; METEO-FRANCE, CNRM/GMME/PHY-NH<br>Bouniol, Dominique; Météo-France/CNRS, CNRM/GAME |
| Keywords: | Regional and mesoscale modelling < 1. Tools and methods, Mesoscale < 2. Scale, Convection < 3. Physical phenomenon, Ice/icing < 3. Physical phenomenon, Microphysics < 3. Physical phenomenon, Atmosphere < 4. Geophysical sphere, Tropics < 5. Geographic/climatic zone |
| Country Keywords: | France |
| | |

# Improvements to the parameterization of snow in AROME in the context of ice crystal icing

*Jean Wurtz, Dominique Bouniol, Benoît Vié*

*CNRM, Université de Toulouse, Météo-France, CNRS, Toulouse, France*

*Corresponding author: Jean Wurtz, CNRM - Météo-France, 42 avenue Gaspard Coriolis, 31057 Toulouse, France.* *email: jean.wurtz@meteo.fr*

*Keywords: Mesoscale modelling, ice/icing, convection, microphysics, atmosphere*

*Funding: None*

**Abstract:**

Ice crystal icing (ICI) poses a threat nowadays for airplane pilots crossing the anvil of tropical meso-scale convective systems (MCS). The use of fine scale operational numerical weather predictions as provided by the French limited area model AROME could help to better understand this phenomenon and to help its anticipation. To enable AROME to simulate ICI-prone conditions, modifications of its single moment microphysical scheme ICE3 are tested. Using a temperature dependent snow particle distribution deeply impacts the organization and the ice phase of the simulated MCS. Notably, while the size of convective regions decreases, the size of anvil clouds increases and the low stratiform rain increases as well. As a result, by increasing the quantity of snow and decreasing the quantity of graupel the simulation of ICI-prone conditions in the anvil of convective systems is enabled. Using this parameterization, further modifications fine-tune the representation of snow and further increase the size of the anvil cloud. The Marshall-Palmer snow distribution is replaced by a generalized gamma and the terminal fall velocities of snow hydrometeors are parameterized so that they are in closer agreement with observations.

# 1) Introduction

As early as 1963, Simpson (1963) reported icing on aircrafts at temperatures as low as -60°C. At such temperatures icing cannot be caused by the presence of supercooled liquid water (Bernstein and Le Bot, 2009; DeMott and Rogers, 1990; Heymsfield and Miloshevich, 1993; Schaefer, 1962) and hence was necessarily due to ice crystals. Later, during the 90's, multiple flight incidents due to the accretion of ice on the engines or on the aircrafts' instruments occurred at relatively high altitudes in low air temperatures (between -27°C and -33°C), and mainly while aircrafts were cruising in the stratiform regions of the convective system considered as safe (Lawson et al., 1998). Inquiries based on pilots' reports helped to comprehend the cloud microphysical characteristics and the environmental weather conditions of these events (Bravin and Strapp, 2019; Grzych and Mason, 2010; Mason et al., 2006; Mason and Grzych, 2011). They concluded that high ice water contents (IWC) of relatively small ice particles in high concentrations are responsible for these incidents. Such ice particles, when hitting the aircraft's engines or its instrumentation, can melt due to the heat released by friction or by the engines, and freeze thereafter, leading to ice accretion as time goes on (Mason et al., 2006). This unavoidable threat is denoted as ice crystal icing (ICI) and is mainly found in the anvil of mature to decaying tropical MCS. Unfortunately, these conditions can not be detected by pilots using their on-board instruments. Indeed, X-band (~9GHz) reflectivities higher than the 30 dBz threshold, considered as hazardous by pilots, are not encountered in the case of high ice water contents (IWC) in anvil clouds (Proctor et al., 2017). Satellite based pre-warning and now-casting systems are beginning to be used and their developments are still ongoing (Haggerty et al., 2019, 2020). The use of operational meso-scale convection permitting simulations should help to further improve our knowledge of the physical processes leading to ICI prone conditions. Using the MetOffice Unified Model (Walters et al., 2017), Franklin et al., (2016) found a too-high proportion of high reflectivities above the melting level compared to the observed frequency during the 2014 Darwin airborne HAIC field campaign. In their simulations, high IWC and the sustainability of the stratiform anvil were found to be sensitive to graupel growth, warm rain processes and modifications to the dynamics and the turbulence scheme. Using either a one (WSM6 (Hong and Lim, 2006)), a two moment microphysical scheme (Morrison et al., 2009) or the P3 microphysical scheme (Morrison and Milbrandt, 2015), Huang et al. (2020) also found that the radar reflectivities were generally overestimated above the melting level. Nevertheless, using a single moment bulk scheme in a large eddy simulation, (Proctor et al., 2017) found that it was possible to simulate anvil clouds with high and sustained IWC with below 30dBz reflectivities. The skills of the operational meso-scale system AROME have been assessed by (Wurtz et al., 2021) using the French-Guiana HAIC 2015 airborne field campaign. This study suggests that revisions to

the microphysical scheme ICE3 are necessary to enable the simulation of high and sustained ice water content (IWC), favorable to ICI, in anvil clouds.

This present study aims to explore several possibilities for the enhancing of the microphysical parameterization of AROME in the context of ICI. A detailed analysis of the resulting alteration in the convective, the stratiform and cirriform regions of the cloud microphysical composition is performed on the HAIC field campaign period and a case study is analyzed to better understand the microphysical processes leading to such conditions. In this study, behaviors in the convective region and in the anvil cloud (stratiform and cirriform regions) of the MCS are analyzed separately using the contextualization of convective systems based on dynamics and precipitation rates of Wurtz et al. (2021). Convective regions are either identified by maximum vertical velocities higher than $2.5 m.s^{-1}$ or by rainfall rates higher than $15 mm.h^{-1}$, stratiform regions are non-convective regions where rainfall rates exceeds $1 mm.h^{-1}$ and cirriform regions are non-stratiform regions where ice water paths exceed $0.5\ kg.m^{-2}$.

The following section describes the model AROME and more specifically its microphysical scheme ICE3. Section 3 is dedicated to the description of tests while section 4 describes the changes induced in the microphysical processes in a case study. Section 5 details the modifications of the organization of MCS and cloud composition statistically.

## 2) The French mesoscale forecast system AROME and its microphysical scheme ICE3

The AROME model (Brousseau et al., 2016; Seity et al., 2011) is a non-hydrostatic limited area model used by the French operational meteorological service for up to 48-h forecasts. AROME implements fine descriptions of atmospheric and surface physics. It shares its package of physical parameterizations with the Mesoscale Non-Hydrostatic (Meso-NH) French research model (Lac et al., 2018), and its dynamical core with Aladin-NH (Bubnová et al., 1995).

Deep convection movements are permitted and shallow convection is parameterized following (Pergaud et al., 2009). A radiation scheme based on Mlawer et al. (1997), Fouquart and Bonnel (1980) and Morcrette (1991) is used to describe atmospheric radiative transfer. The atmospheric turbulence is represented by a one dimension scheme, so without any horizontal mixing, based on a prognostic equation of Turbulent Kinetic Energy (Cuxart et al., 2000).

The state of the ocean surface greatly influences not only cloud organization and the life cycle of low clouds (Chung et al., 2012; Klein and Hartmann, 1993), but also that of deep convective clouds (Costa et al., 2001). The coupling with oceanic surface is performed by a 1D column model (Lebeaupin Brossier, 2007) initialized by the MERCATOR PSY4 ocean model at a resolution of 1/12° (Lellouche et al., 2018). Interactions between continental surfaces and atmosphere are described by the surface scheme SURface Externalisée (SURFEX, (Masson et al., 2013)).

AROME not only operates in France and continental Europe but also overseas (Faure et al., 2020). A specific AROME domain of approximately 1200 km length and 900 km width is implemented in French Guiana. The simulation domain includes a large fraction of oceanic surface (~70%). The model is run with its operational setup: a 60 second time step and a 2.5km horizontal resolution. The vertical dimension extends from ~5m up to ~34 km using 90 vertical levels, most of them located near the surface and involving a vertical resolution decrease overhead from 10m close to the surface to 100m at the top of the mixing layer and roughly 400m at a height of 10km.

As in Wurtz et al.(2021), the initial and forcing conditions for the simulations performed in this study are provided by ARPEGE (Action de Recherche Petite Echelle Grande Echelle, (Courtier et al., 1991)), the French operational global forecast system.

The incremental analysis update algorithm from (Bloom et al., (1996) is used to reduce model spin-up. An initial AROME run beginning at 18UTC the day before is used to initialize water related variables at the 00UTC. Nevertheless, spin-up can still influence the results of cloud microphysics during the very first hours of forecast. The first three hours of simulations are therefore not considered. In this study, 24 hours AROME simulations with hourly outputs are performed starting

from 00UTC between May 09, 2015 and May 29, 2015 and corresponding to the operation period of the Falcon-20 during the HAIC field campaign of 2015.

The operational model AROME implements the ICE3 single moment bulk microphysical scheme (Pinty and Jabouille, 1998; Riette, 2020). In addition to the water vapor, cloud microphysics are represented using three ice species (pristine ice, snow which typically represents crystal larger than 200µm and graupel representing dense ice) and two liquid water species (cloud droplets and rain drops). Pristine ice and cloud droplets are the first to form due to condensation based on a saturation adjustment using the works of Lord et al. (1984) and Tao et al. (1989). The warm liquid phase is described by the Kessler (1969) scheme. For each hydrometeor type the only prognostic variable is the mass mixing ratio. Each hydrometeor is described using mass-diameter and terminal fall velocity – diameter relationships expressed as power-laws taken from Locatelli and Hobbs (1974) and Heymsfield (1972) for ice hydrometeors. These laws are defined by two couples of values (a, b) and (c, d) which differ for each ice species, the values of which are provided in Table I.

A generalized gamma distribution is used to represent the particle size distribution (PSD) of each hydrometeor:

$$n(D) = N_t \cdot \frac{\alpha}{\Gamma(\nu)} \lambda^{\alpha\nu} D^{\alpha\nu-1} \exp\left(-(\lambda D)^{\alpha}\right) \qquad (1)$$

Here, $N_t$ is the total number concentration of the described species and α, ν are known as shape parameters for the different species (see Table I). α and ν are set to 1 for precipitating species and such a PSD shape is known as a Marshall-Palmer (MP) law (Marshall and Palmer, 1948). The PSD of snow species could however be better described using a generalized gamma law (Wurtz et al., 2021).

The λ parameter is physically linked to the proportion of small versus large hydrometeors: the higher the λ, the higher proportion of small hydrometeors. Cloud liquid water PSD is set differently based on the surface type (oceanic or continental) underneath the cloud in order to indirectly take into account the population of cloud condensation nuclei (Albrecht, 1989; Hudson and Yum, 2001). As a result, different values for α and ν depending on the surface type are chosen (see Table I) and the cloud droplet number concentration takes the constant value of $3\text{x}10^8$ and $1\text{x}10^8$ $\text{m}^{-3}$ over land and sea areas, respectively.

For snow, graupel and rain, the total number concentration $N_t$ ($\text{m}^{-3}$) is linked to the mass mixing ratio $r$ (in $\text{kg.m}^{-3}$) through Equation 2:

$$N_t = \frac{r\lambda^b}{aG(\alpha,\nu,b)} \quad (2)$$

with:

$$G\left(\alpha,\nu,b\right) = \frac{\Gamma\left(\nu+\frac{b}{\alpha}\right)}{\Gamma\left(\nu\right)} \quad (3)$$

As ICE3 is a single moment scheme a closure assumption on $N_t$ or on λ is needed to completely describe the PSD. Using a MP law, Passarelli (1978) proposed to link $N_t$ to λ through a power law for snow such as:

$$N_t = C\lambda^x \quad (4)$$

Different values of $C$ and $x$ can be found in the literature for snow (Passarelli, 1978), graupel (Cheng et al., 1985; Cheng and English, 1983) or rain (Marshall and Palmer, 1948) species. Caniaux (1993) tested multiple values of $C$ and $x$ in ICE3. Among them, the values given in Table I are used in the operational version of AROME.

Using Equation 2 in Equation 4 gives:

$$\lambda = \left(\frac{aCG\left(\alpha,\nu,b\right)}{r}\right)^{\frac{1}{b-x}} \quad (5)$$

For precipitating ice species, the whole PSD can be deduced from the only prognostic variable $r$. Nevertheless, comparing this parameterization to observations suggests that adjustments to the parameterization of λ are necessary (Wurtz et al., 2021).

For pristine ice, the computation of $N_t$ is based on the supersaturation over ice (Meyers et al., 1992). The auto-conversion of pristine ice to snow is allowed when it reaches a mass content threshold dependent on the air temperature (Chaboureau and Pinty, 2006; Ryan, 2000).

Collection and sedimentation processes are described in the Appendix.

TWC ($g.m^{-3}$) in AROME is defined as the sum of all condensed species mass content per volume unit.

## 3) Description of sensitivity tests

Aggregates represent a great part of ice water content in anvil clouds. These aggregates are represented in ICE3 by the snow category and represent indeed the majority of ice content in simulated anvil clouds. Following Wurtz et al. (2021) different experiments were launched using the modifications described hereafter and are summed up in Table III. These modifications are based on diagnostics derived from observations.

## 3.1) Parameterization of the PSD of snow

Wurtz et al. (2021) demonstrated that the closure equation linking $N$ to λ does not well describe the observed behavior of λ sampled during the HAIC field campaign. Moreover, the authors showed that the operational version of ICE3 overestimates the size of snow crystals and that using a temperature dependent λ better diagnoses the snow number concentration and the snow PSD. Indeed, the size of snow crystals increases as they fall due to the deposition and aggregation processes (Mitchell, 1988). As a result, it is proposed rather on the advice of Heymsfield (2003) and Houze et al. (1979) to parameterize λ as a function of temperature using the following equation:

$$\lambda(T) = 10^{A-BT} \tag{6}$$

where $T$ is in Kelvin and λ in $m^{-1}$. This new closure assumption enables the derivation of the total number concentration of snow hydrometeors by using Equation 2 and avoids the use of Equation 4. $A$ and $B$ coefficients need however to be determined. $B$ coefficient is the slope (in log scale) and represents the result of aggregation, deposition and the selection of the largest crystals by sedimentation as a function of height (or temperature). $A$ coefficient can be adapted to parameter $B$ in order to set the minimal value of λ (for 273.15K) close to $1000m^{-1}$, which can be considered as a lower limit as shown by Lo and Passarelli (1982) and Lo (1983).

As demonstrated by Heymsfield (2003), or for the HAIC dataset by (Wurtz et al., (2021), the variability of λ from cloud to cloud is high. Hence different $\lambda(T)$ parameterizations can be derived depending on the data set. Two different sets of parameters are tested in the following. The first tested ($A$, $B$) couple has been derived by (Houze et al., (1979) on mid-latitudes fronts for temperatures between 0°C to about -43°C and is set to (9.006, 0.022). Heymsfield (2003) proposed two couples of ($A$, $B$) values depending on the two temperature ranges: above and below -10°C. Following this study, two specific ($A$, $B$) couples to HAIC field campaign have been derived using the median λ of the three sampled temperature levels (-10°C, -30°C and -45°C) (Wurtz et al., 2021). The value of $1000m^{-1}$ is chosen as the lower limit for λ at 273K (Lo and Passarelli, 1982; Lo, 1983),

and the law can be extrapolated between 0°C and -10°C. As a result, ($A$, $B$) couple is set to (14.554, 0.0423) for temperatures above 263K and to (6.226, 0.0106) for temperatures below this threshold.

These laws are shown in Figure 1. For temperatures lower than -30°C, the λ derived from Houze et al. (1979) is higher than that derived from the HAIC dataset, and it is lower for temperatures higher than -30°C. The law derived by Heymsfield (2003) is not tested hereafter to avoid too many and too similar tests, but this relationship gives even higher λ values for temperatures lower than -10°C. Figure 1 also shows that although the linear regression is limited to three points for HAIC dataset and hence confidence in this regression is limited, the magnitude of λ computed is consistent with the datasets of Heymsfield (2003) and Houze et al. (1979) datasets.

Hereafter these two experiments are denoted as HAIC-MP and HOUZE-MP (see Table III).

In addition, the λ-T parameterization enables the use of a generalized gamma law which has been proven more accurate to describe the PSD of snow (Elsaesser et al., 2017; Wurtz et al., 2021) but which was not adapted to the N(λ) closure assumption (Equation 4).

To ease its implementation in AROME, the shape was fixed to the best compromise derived by Wurtz et al. (2021): α = 0.214, ν = 43.7. To use the λ-T parameterizations which are derived for a MP shape, the value of λ parameter has to be adapted to the shape of the distribution with a constant factor. This factor can be derived using the moments of the distribution. Indeed moment $n$ of the distribution can be computed using (where $G$ is defined in Equation 3):

$$M(n) = \frac{G(\alpha, \nu, b)}{\lambda^n} \tag{7}$$

Using moments from 1 to 4 gives the following relationship:

$$\lambda(\alpha, \nu) = \lambda_{MP} \cdot \frac{1}{2\sqrt{2}} \cdot \sqrt{\frac{\Gamma(\nu + 2/\alpha)\Gamma(\nu + 4/\alpha)}{\Gamma(\nu + 1/\alpha)\Gamma(\nu + 3/\alpha)}} \tag{8}$$

Figure 2 compares the generalized gamma shape (α = 0.214, ν = 43.7) to the MP using the same concentration and λ parameters. The number of big and small aggregates are respectively increased and decreased and a mode appears for snow crystals of a few hundreds of µm. In the following, several experiments use a generalized gamma law which is indicated by "GG" (HAIC-GG, and HAIC-GG-Vt: see Table III for more details).

## 3.2) Modification of the terminal velocities – diameter relationship

In AROME, the terminal fall speed is parameterized using a power law relationship corrected by a factor taking into account the air density (Foote and Du Toit, 1969):

$$v(D) = cD^d \cdot \left(\frac{\rho_0}{\rho}\right)^{0.4} \quad (9)$$

where $\rho$ is the density of dry air, $\rho_0$ the density of dry air at the reference pressure and temperature of 1013.15hPa and 20°C and equals 1.204kg.m$^{-3}$. In the operational version, parameters $c$ and $d$ are taken from Locatelli and Hobbs (1974) (L&H in the following) and correspond to the category described as "aggregates of densely rimed radiating assemblages of dendrites or dendrites" with diameters ranging from 2000 µm to 12 000µm (Table II). This range of diameters is extrapolated for the terminal fall speed of smaller snow hydrometeors. L&H describes the terminal fall speed of an "aggregates of unrimed radiating assemblages of plates, side planes, bullets, and columns" category where the diameters span between 200µm and 3000µm (Table II).

Using multiple laws for different ranges of diameters is not convenient for a bulk microphysical scheme. In particular, it would unreasonably increase the computation cost. In order to extend the validity of the parameterization for a larger range of diameters, Ferrier (1994) (for raindrops only) and Thompson et al. (2008) add an exponential factor, $f$, in Equation 9:

$$v(D) = cD^d exp(-fD) \cdot \left(\frac{\rho_0}{\rho}\right)^{0.4} \quad (10)$$

Equation 10 enables the easy computation of moments and extends the validity range of the terminal velocity law. Nevertheless, this parameterization has been derived to be used with a gamma shape ($\alpha = 1$). As inspired by these articles, an extension of this exponential factor is proposed for generalized gamma laws where $\alpha \neq 1$:

$$v(D) = c_\alpha D^{d_\alpha} \cdot exp(-(f_\alpha D)^\alpha) \cdot \left(\frac{\rho_0}{\rho}\right)^{0.4} \quad (11)$$

Even so, as the law has been modified and in order to keep realistic terminal fall velocities, one has to note that here the $c_\alpha$, $d_\alpha$ and $f_\alpha$ parameters are now dependent on the choice made on α. This dependency to $\alpha$has been made in order to ease the computation of moments where terminal fall velocities are used.

To derive the $c_\alpha$, $d_\alpha$ and $f_\alpha$ parameters of this extended parameterization (Equation 11), the parameters of this law enabling the concatenation to be the closest of the two original laws of L&H are selected. In order for this to happen, an extended version of the quasi-Newton method

"Broyden-Fletcher-Goldfarb-Shanno" is used (Guitton and Symes, 2003). Table II gives the various $c_\alpha$, $d_\alpha$ and $f_\alpha$ parameters found for the MP shape and the generalized gamma shape and a graphical comparison is proposed in Erreur : source de la référence non trouvée. The laws for the MP and the generalized gamma shapes can be considered as extended versions of the L&H parameterization. Compared to the L&H law designed for large aggregates operationally used in AROME and extrapolated to smaller hydrometeors, terminal fall velocities of the extended L&H parameterization are lower for relatively small snow crystals.

The impact of using this extended L&H parameterization for terminal fall velocities is tested in three experiments: Vt (only the terminal fall velocity formulation is changed), HAIC-MP-Vt (using the HAIC λ-T relationship with the extended L&H parameterization and a MP PSD), HAIC-GG-Vt (same as the previous experiment but assuming a generalized gamma shape for PSD).

## 4) Detailed analysis of changes in the sensitivity tests: Case study of 29 May 2015

The impact of the proposed changes on the microphysical processes is first explored in detail using a case study from the HAIC 2015 field campaign: the 29 May 2015 MCS. GOES-13 infra-red brightness temperatures for this MCS are shown at three different life stages in Figure 4. The convection is well organized, long-lived and slow moving. As shown in (Figure 5a), ICI-prone conditions, with high and sustained ice water contents in a relatively low air temperature, were sampled in the anvil cloud of this MCS, and especially in the stratiform region (green filled contours in Figure 5). This MCS is well simulated by the operational AROME model (Figure 5b), however no ICI-prone conditions could be simulated by this operational version where all high ice water contents are confined to the convective towers (yellow filled contours in Figure 5). Changing only the terminal fall speed law (MP-Vt), does not lead to ICI-prone conditions (not shown). On the contrary, in simulations where the λ-T relationships are implemented (all HAIC experiments or HOUZE-MP), the extension of high ice water contents within the anvil cloud and the stratiform region is much higher (Figure 5c), which is more consistent with the observations (Figure 5a). As a result, all simulations where a λ-T relationship is implemented, are able to simulate ICI prone conditions (not shown).

Figure 6 compares the cloud composition of OPER and HAIC-MP experiments while microphysical mass tendencies are presented in Figure 7. Collection processes are represented by dotted curves. The tendencies for other experiments with a λ-T relationships (HOUZE-MP or HAIC with MP, GG or Vt attributes, *cf.* Table III) are close to the HAIC-MP experiment and hence not shown.

As shown in Figure 6a, in OPER, the convective region is mainly composed by graupel hydrometeors at temperatures higher than -20°C while more snow is found for temperatures colder than -20°C. In this region, vertical movements favor the transportation of liquid hydrometeors to altitudes where temperatures are below 0°C, lift ice hydrometeors including graupel, favor collection processes and increase relative humidity up to supersaturated levels thus pristine ice can form. As a result, collection processes, including the collection of liquid water, are very active in this region (riming, accretion, wet and dry growth of graupel, see Figure 7) and a lot of graupel is formed. A large part of the formed pristine ice is converted into snow first by auto-conversion and when there is enough snow, more efficiently by aggregation (Figure 7). Part of auto-conversion and aggregation can be seen here as indirect water vapor deposition on snow as it is in inhibited by the saturation adjustment which only forms pristine ice or cloud droplets.

The stratiform region is dominated by snow hydrometeors (Figure 6b) and large amounts of graupel are only found in the lower region of the ice cloud. A great part of this ice has sedimented, especially graupel which falls rapidly. Pristine ice and snow fall more slowly and can be detrained further away. In addition, the detrained pristine ice can easily form snow by auto-conversion and aggregation. The behavior of microphysical processes in the stratiform region differ quite a lot from the convective region in particular because vertical movements are much weaker. As a consequence, collection processes are much less efficient, and the impact of riming and accretion above all is negligible (Figure 7). As a result, less graupel is formed which again decreases collection efficiency. In the cirriform region (Figure 6c), ice water contents are lower than in the stratiform region, especially in the lower region of the cloud, while the upper region is maintained thanks to a radiative instability (Gasparini et al., 2019). Active microphysical processes in the cirriform region are similar to those of the stratiform region but with lower mass tendencies and are hence not shown.

The cloud composition (Figure 6) and the behavior of microphysical processes (Figure 7) are deeply modified in the HAIC-MP experiment compared to that of the OPER experiment. Indeed, using the λ-T parameterization, both the λ parameter and snow concentration are more realistic, which impacts the collection (see Appendix A1) and sedimentation processes (see Appendix A2).

In the convective region, less graupel and more pristine ice is found in HAIC-MP when compared to OPER and snow contents are higher at temperatures colder than -10°C, but lower at warmer temperatures. This is can be explained by snow collection processes, which are significantly reduced, except for the wet growth of graupel which may be influenced by the melting of more snow (Figure 7). Hence, generally less snow is converted into graupel and thus more snow remains.

As a result, more snow can be detrained in the stratiform and cirriform regions resulting in larger stratiform and cirriform regions as shown in Figure 5. Snow contents are therefore also much higher. This increases both sedimentation rates (Figure 7) and number concentration, which induces a higher sublimation rate (Figure 7).

It may be remarked that, however shown has a key process in these convective clouds (Ackerman et al., 2015; Korolev et al., 2020; Leroy et al., 2017), deposition remains negative (sublimation) due to the saturation adjustment performed in ICE3 which disables the possibility of high supersaturation and realistic deposition. In our case, all water vapor available for condensation can condensate and hence can form the expected high ice water contents even with a single moment microphysical scheme (Figures 6 and 8).

Then again, graupel contents are lower because the dry growth is less effective (Figure 7). At the same time, the wet growth of graupel in the region where the temperature is close to 0°C is higher as more snow melts forming graupel and liquid water after complete melting which can also be converted into graupel after collection. Pristine ice is less impacted. Slightly less is found for temperatures higher than -30°C while slightly more is found at temperatures lower than -30°C. Overall, total ice water contents are increased in HAIC-MP (Figure 6).

In the context of ICI, the formation of high ice water contents in the anvil cloud is thus highly impacted by the possibility of maintaining ice water in the stratiform region and impacted by what type of ice is created in the convective region. The more snow and pristine ice is created in the convective region, the higher the number concentration (which is true for a λ-T parameterization, see Equation 2) and the more easily it can be detrained in the anvil cloud. For this reason, the formation of less graupel in the convective region favors the creation of more snow and thus results in higher ice water content in the anvil cloud. In the stratiform region, lower terminal fall velocities also help to maintain this ice water.

## 5) Analysis of the sensitivity tests for the HAIC-2015 period

As shown in the precedent case study, the changes induced by the λ-T parameterization result in deep changes in the MCS cloud organization (Figure 5), cloud composition (Figure 6) and microphysical processes (Figure 7). In this section, a statistical study is performed on the entire period from May 10 2015 to May 29 2015 in French Guiana to assess the modifications induced by this λ-T parameterization and by the other proposed changes. This period corresponds to the HAIC 2015 field campaign period where 15 flights were performed during 13 flight days.

Weather conditions favoring ICI correspond to high total water contents (TWC) on large areas in anvil clouds in a relatively low temperature air and without supercooled water (see Introduction). To have the closest comparison as possible, each simulated MCS corresponding to a sampled MCS during the HAIC-2015 field campaign is selected. This sample of simulated MCS is composed with 137 hourly outputs. ICI-prone conditions are identified in AROME by focusing on high and sustained TWC at relatively low temperatures. To this effect, $Spread$ is defined to measure the dispersion within the studied clouds as:

$$Spread = \log_{10}\left(percentile_{90}\left(TWC\right)\right) - \log_{10}\left(percentile_{10}\left(TWC\right)\right) \quad (12)$$

As a result, high median TWC and low $Spread$ clouds identify ICI-prone conditions. Using these measures, each dot shown in Figure 8 is representative of each region of a simulated MCS. In this Figure 8, dots in the lower-right region of each graph correspond to ICI-prone conditions, especially those with colder temperatures. Dots where median TWC is superior to 0.5 $g.m^{-3}$ and where temperatures are equal to or below -30°C are larger, indicating a ICI possibility. Each observed case represents a flight segment and the results for observations of Figure 8 are taken from Wurtz et al. (2021).

Contrary to what has been sampled during the 2015 HAIC field campaign, very few ICI favorable conditions were simulated in OPER (Wurtz et al., 2021) and Vt (not shown). Nevertheless, in the HAIC experiment, many more ICI-prone conditions are simulated (Figure 8). Median TWC can be even larger than 1 $g.m^{-3}$ with a reduced spread even at temperatures below -30°C.

Actually the proposed modifications impact the horizontal size of each region of the MCS (Table IV), the distribution of rainfall rates within the stratiform region (Figure 9) and the mean cloud composition (Figures 10 and 11). Few effects were observed however on the life cycle of these simulated MCS. Table IV informs one of the changes in the total area of each sub-region of MCS for each experiment compared to OPER. Figure 9 shows the distribution of rainfall rate in the stratiform region normalized by the total stratiform area for each experiment. Such a diagnostic has

also been performed for the convective region but no changes were observed (not shown). Figure 10 gives the vertical mean cloud composition.

In the Vt experiment, the size of convective region increases while the size of the anvil cloud decreases (Table IV). Clouds are composed of less snow, less graupel and more pristine ice compared to OPER, as the reduced fall velocity decreases the collection of snow and less pristine ice is converted to snow (Figure 10). However, few changes can be observed on stratiform rainfall rates (Figure 9)

With a temperature dependent λ (all HAIC experiments and HOUZE-MP), the size of the convective region decreases while that of anvil cloud increases. In particular, while convective regions cover a total area 8% smaller than in OPER, the stratiform and cirriform clouds are broader by ~30% in HAIC-MP compared to OPER. In addition, low rainfall rates in the stratiform region increase and high ones decrease (Figure 9). As shown in the case-study, the microphysical composition of each sub-region is deeply modified in HAIC (Figure 10), as more snow and less graupel are found compared to OPER. These changes can be explained by the modifications of sedimentation and by the decrease in efficiency of the collection processes as observed in our case study. Indeed, the fall of snow is slower and formation of graupel by collection processes is reduced, so more snow subsists and more snow can be detrained. Compared to the OPER experiment, more pristine ice is found in the convective region and in the upper region of stratiform and cirriform regions of the HAIC experiment. Meanwhile, less pristine ice is found in the lower regions.

All these experiments using a temperature dependent λ have similar impacts on the mean cloud composition compared to OPER. That is why they are all compared to the HAIC-MP experiment in Figure 11.

Changing the λ-T parameterization from HAIC to HOUZE impacts the snow content in the stratiform region (Figure 11). Looking at both Figure 11b and Figure 1, it seems that a link exists between the difference in λ and the difference in snow content in stratiform and cirriform regions. For temperatures lower than -30°C, λ is higher in HOUZE compared to HAIC, and lower at temperatures higher than -30°C (Figure 1). At the same time (Figure 11)., snow contents are higher at temperatures lower than -30°C and lower at temperatures higher than -30°C. So it seems that the higher the λ, the higher the proportion of small snow hydrometeors and the slower snow falls, hence more hydrometeors are maintained in the anvil.

Using a generalized gamma shape (HAIC-GG) mainly impacts the lower region (between 0°C and -20°C) of the convective and stratiform regions where snow contents are almost divided in half

(Figure 11). At the same time, the pristine ice content is slightly higher. Higher in the stratiform and cirriform regions however, graupel contents remain low. In fact, more large crystals are represented using the generalized gamma shape (see Figure 2), and especially so for low λ at relatively warm temperatures. Hence, fall velocities for these large crystals are higher and it impacts snow sedimentation and the collection processes resulting in more graupel.

Extending the validity of the terminal fall velocities parameterization (HAIC-MP-Vt) has more impact on the upper region of the anvil cloud (Figure 11). Indeed, snow particles are smaller there and fall more slowly with this modification and hence accumulate aloft. At warmer temperatures, snow particles are bigger and there are no differences in fall velocity with the proposed modification.

The HAIC-GG-Vt simulation generally sums up the effects of GG and Vt especially for snow in the convective and stratiform regions (Figure 11). And while less significant individually, the sums of the two modifications can be more easily felt. Indeed, GG and Vt modifications to the HAIC experiment further decrease the terminal fall velocity of snow and hence snow can be transported further away from the convective region. This can be felt especially in HAIC-GG-Vt where the stratiform area increased by ~40% and the cirriform area by ~70% (Table IV). When compared to HAIC-MP, low rainfall rates increase further and high rainfall rates decrease further (Figure 9).

Overall, all simulations using a temperature dependent λ (HOUZE-MP, HAIC-GG, HAIC-MP-Vt, HAIC-GG-Vt) are, as in the HAIC-MP experiment (Figure 8), able to simulate ICI conditions for the same cases, but with an intensity and a frequency that may slightly vary from case to case (not shown) especially because stratiform and cirriform regions are broader (Table IV) and snow contents higher in altitude (Figure 11). In particular, GG and Vt slightly increase the ICI frequency and intensity.

## 6) Conclusion and outlook

The sensitivity tests performed in this study show that the meso-scale forecast system AROME using the single moment microphysical scheme ICE3 is able to simulate ICI-prone conditions if the parameterization of the snow distribution is modified using a temperature-dependent λ. This modification has a great impact on the simulated microphysical processes, and especially on sedimentation and collection processes. Actually, the snow content significantly increases while graupel content decreases. As a result, the size of convective regions decreases while the size of the anvil cloud increases. Simultaneously, the rainfall rates in the stratiform regions are generally lower. This shows that, additionally to the tuning of parameters such as collection efficiency parameters or terminal fall velocities parameters, the PSD can have a great influence on the microphysical processes, cloud organization and composition. As several temperature-dependent λ laws can be derived with different dataset, sensitivity to the law has been tested. Impacts with a different law were similar compared to HAIC, and higher λ implies higher snow contents.

Further refinements such as parameterizing the snow PSD shape by a generalized gamma and better representing the snow terminal velocities fine-tune the microphysical description of snow. In particular, it further increases the extent of the anvil cloud and of weak stratiform rains, and hence the number and the intensity of ICI-prone conditions.

More sensitivity tests could be performed to improve the microphysics of the cloud anvil and could help to better understand the formation of ICI conditions. Firstly, a more physically based approach to compute λ could be used (Lo, 1983; Mitchell, 1991, 1988; Passarelli, 1978) or the use of a two moment scheme such as LIMA (Vié et al., 2016) may be more realistic. In particular it enables to take into account secondary ice processes (Ackerman et al., 2015; Huang et al., 2022; Korolev et al., 2020) which are important to compute deposition process explicitly which seems an essential process in these clouds (Ackerman et al., 2015; Korolev et al., 2020; Leroy et al., 2017).

The uncertainty of terminal fall velocity is relatively high as well (Heymsfield et al., 2013) and further adjustments could be performed which might have more impact on the behavior of clouds than what has been tested in this study.

In addition to further studies on microphysics, studying turbulence (Franklin et al., 2016) and radiative processes (Wall et al., 2020) and their interactions with microphysics may improve our knowledge on anvil clouds and the forecast skills of AROME, especially for ICI.

Overall, this study paves the way to the investigation of the processes leading to ICI, of the variability of ICI-prone conditions and to the development of diagnostics using the AROME operational model or other similar models.

460

# APPENDIX

## A.1) Collection in ICE3

Collection processes between two species $x$ and $y$ in ICE3 are parameterized using the general collection parameter $K$ [m$^3$.s$^{-1}$] parameterizing mutual gravitational interaction:

$$K(D_x, D_y) = \pi/4(D_x + D_y)^2 |v_x(D_x) - v_y(D_y)| E_{xy} \quad \text{(A.1.13)}$$

where $D$ is the diameter [m] of hydrometeors, $v$ the terminal fall velocity [m.s$^{-1}$] and $E_{xy}$ the collection efficiency.

The mass tendency $\frac{\partial r_{z_{collection}}}{\partial t}(x, y)$ [kg.kg$^{-1}$.s$^{-1}$] of collection of $x$ by $y$ to form $z$ can be expressed by the integration of the total mass collected:

$$\frac{\partial r_{z_{collection}}}{\partial t}(x, y) = 1/\rho \int_0^{+\infty} [\int_0^{+\infty} n(D_y) m(D_y) K(D_x, D_y) dD_y] n(D_x) dD_x \quad \text{(A.1.14)}$$

Where $\rho$ [kg.m$^{-3}$] is the density of dry air.

## A.2) Sedimentation in ICE3

Sedimentation in AROME uses the statistical method of (Bouteloup et al., 2011). Sedimentation mass flux $\phi_{SEDIM}$ [kg.m$^{-2}$.s$^{-1}$] is computed by the integration of the sedimentation mass flux of each hydrometeor on the whole distribution

$$\begin{aligned} \phi_{SEDIM} &= \int_0^{+\infty} n(D) m(D) v(D) dD \\ &= ac(\rho_0/\rho)^{0.4} \cdot M(b + d) \end{aligned} \quad \text{(A.2.1)}$$

where $a$ and $b$ are parameters from the mass-diameter law and $c$ and $d$ from the terminal fall velocity-diameter law (see Equation 9) and values can be found in Table I. $\rho$ is the dry air density and $\rho_0$ is the density of dry air at the reference pressure and temperature of 1013.15hPa and 20°C and equals 1.204 kg.m$^{-3}$.

## Bibliography:


Ackerman, A., Fridlind, A., Grandin, A., Dezitter, F., Weber, M., Strapp, J., Korolev, A., 2015. High Ice Water Content at Low Radar Reflectivity near Deep Convection: Part II. Evaluation of Microphysical Pathways in Updraft Parcel Simulations.

Albrecht, B.A., 1989. Aerosols, cloud microphysics, and fractional cloudiness. Science 245, 1227–1230.

Bernstein, B.C., Le Bot, C., 2009. An inferred climatology of icing conditions aloft, including supercooled large drops. Part II: Europe, Asia, and the globe. J. Appl. Meteorol. Climatol. 48, 1503–1526.

Bloom, S., Takacs, L., Da Silva, A., Ledvina, D., 1996. Data assimilation using incremental analysis updates. Mon. Weather Rev. 124, 1256–1271.

Bouteloup, Y., Seity, Y., Bazile, E., 2011. Description of the sedimentation scheme used operationally in all Météo-France NWP models. Tellus A 63, 300–311. https://doi.org/10.1111/j.1600-0870.2010.00484.x

Bravin, M., Strapp, J.W., 2019. A continuing investigation of diurnal and location trends in an ice crystal icing engine event database. SAE Int. J. Adv. Curr. Pract. Mobil. 2, 90–105.

Brousseau, P., Seity, Y., Ricard, D., Léger, J., 2016. Improvement of the forecast of convective activity from the AROME-France system. Q. J. R. Meteorol. Soc. 142, 2231–2243.

Bubnová, R., Hello, G., Bénard, P., Geleyn, J.-F., 1995. Integration of the fully elastic equations cast in the hydrostatic pressure terrain-following coordinate in the framework of the ARPEGE/Aladin NWP system. Mon. Weather Rev. 123, 515–535.

Caniaux, G., 1993. Paramétrisation de la phase glace dans un modèle non hydrostatique de nuage: application à une ligne de grains tropicale (PhD Thesis).

Chaboureau, J.-P., Pinty, J.-P., 2006. Validation of a cirrus parameterization with Meteosat Second Generation observations. Geophys. Res. Lett. 33.

Cheng, L., English, M., 1983. A relationship between hailstone concentration and size. J. Atmospheric Sci. 40, 204–213.

Cheng, L., English, M., Wong, R., 1985. Hailstone Size Distributions and Their Relationship to Storm Thermodynamics. J. Appl. Meteorol. Climatol. 24, 1059–1067. https://doi.org/10.1175/1520-0450(1985)024<1059:HSDATR>2.0.CO;2

Chung, D., Matheou, G., Teixeira, J., 2012. Steady-state large-eddy simulations to study the stratocumulus to shallow cumulus cloud transition. J. Atmospheric Sci. 69, 3264–3276.

Costa, A.A., Cotton, W.R., Walko, R.L., Pielke Sr, R.A., Jiang, H., 2001. SST sensitivities in multiday TOGA COARE cloud-resolving simulations. J. Atmospheric Sci. 58, 253–268.

Courtier, P., Freydier, C., Geleyn, J., Rabier, F., Rochas, M., 1991. The arpege project at météo-france, ecmwf workshop, european center for medium-range weather forecast. Read. Engl.

Cuxart, J., Bougeault, P., Redelsperger, J.-L., 2000. A turbulence scheme allowing for mesoscale and large-eddy simulations. Q. J. R. Meteorol. Soc. 126, 1–30. https://doi.org/10.1002/qj.49712656202

DeMott, P.J., Rogers, D.C., 1990. Freezing nucleation rates of dilute solution droplets measured between- 30 and- 40 C in laboratory simulations of natural clouds. J. Atmospheric Sci. 47, 1056–1064.

Elsaesser, G.S., Del Genio, A.D., Jiang, J.H., van Lier-Walqui, M., 2017. An improved convective ice parameterization for the NASA GISS Global Climate Model and impacts on cloud ice simulation. J. Clim. 30, 317–336.

Faure, G., Chambon, P., Brousseau, P., 2020. Operational Implementation of the AROME Model in the Tropics: Multiscale Validation of Rainfall Forecasts. Weather Forecast. 35, 691–710.

Ferrier, B.S., 1994. A Double-Moment Multiple-Phase Four-Class Bulk Ice Scheme. Part I: Description. J. Atmospheric Sci. 51, 249–280. https://doi.org/10.1175/1520-0469(1994)051<0249:ADMMPF>2.0.CO;2

Foote, G.B., Du Toit, P.S., 1969. Terminal Velocity of Raindrops Aloft. J. Appl. Meteorol. Climatol. 8, 249–253. https://doi.org/10.1175/1520-0450(1969)008<0249:TVORA>2.0.CO;2

Fouquart, Y., Bonnel, B., 1980. Computations of solar heating of the Earth's atmosphere: A new parameterization.

Franklin, C.N., Protat, A., Leroy, D., Fontaine, E., 2016. Controls on phase composition and ice water content in a convection-permitting model simulation of a tropical mesoscale convective system. Atmospheric Chem. Phys. 16, 8767–8789.

Gasparini, B., Blossey, P.N., Hartmann, D.L., Lin, G., Fan, J., 2019. What Drives the Life Cycle of Tropical Anvil Clouds? J. Adv. Model. Earth Syst. 11, 2586–2605.

Grzych, M.L., Mason, J.G., 2010. Weather conditions associated with jet engine power loss and damage due to ingestion of ice particles: What we've learned through 2009, in: 14th Conference on Aviation, Range and Aerospace Meteorology.

Guitton, A., Symes, W.W., 2003. Robust inversion of seismic data using the Huber norm. GEOPHYSICS 68, 1310–1319. https://doi.org/10.1190/1.1598124

Haggerty, J., Defer, E., De Laat, A., Bedka, K., Moisselin, J.-M., Potts, R., Delanoë, J., Parol, F., Grandin, A., Divito, S., 2019. Detecting clouds associated with jet engine ice crystal icing. Bull. Am. Meteorol. Soc. 100, 31–40.

Haggerty, J.A., Rugg, A., Potts, R., Protat, A., Strapp, J.W., Ratvasky, T., Bedka, K., Grandin, A., 2020. Development of a Method to Detect High Ice Water Content Environments Using Machine Learning. J. Atmospheric Ocean. Technol. 37, 641–663.

Heymsfield, A., 1972. Ice Crystal Terminal Velocities. J. Atmospheric Sci. 29, 1348–1357. https://doi.org/10.1175/1520-0469(1972)029<1348:ICTV>2.0.CO;2

Heymsfield, A.J., 2003. Properties of tropical and midlatitude ice cloud particle ensembles. Part II: Applications for mesoscale and climate models. J. Atmospheric Sci. 60, 2592–2611.

Heymsfield, A.J., Miloshevich, L.M., 1993. Homogeneous ice nucleation and supercooled liquid water in orographic wave clouds. J. Atmospheric Sci. 50, 2335–2353.

Heymsfield, A.J., Schmitt, C., Bansemer, A., 2013. Ice Cloud Particle Size Distributions and Pressure-Dependent Terminal Velocities from In Situ Observations at Temperatures from 0° to −86°C. J. Atmospheric Sci. 70, 4123–4154. https://doi.org/10.1175/JAS-D-12-0124.1

Hong, S.-Y., Lim, J.-O.J., 2006. The WRF single-moment 6-class microphysics scheme (WSM6). Asia-Pac. J. Atmospheric Sci. 42, 129–151.

Houze, R.A., Hobbs, P.V., Herzegh, P.H., Parsons, D.B., 1979. Size distributions of precipitation particles in frontal clouds. J. Atmospheric Sci. 36, 156–162.

Huang, Y., Wu, W., McFarquhar, G.M., Wang, X., Morrison, H., Ryzhkov, A., Hu, Y., Wolde, M., Nguyen, C., Schwarzenboeck, A., others, 2020. Microphysical Processes Producing High Ice Water Contents (HIWCs) in Tropical Convective Clouds during the HAIC-HIWC Field Campaign: Evaluation of Simulations Using Bulk Microphysical Schemes. Atmospheric Chem. Phys. Discuss. 1–40.

Huang, Y., Wu, W., McFarquhar, G.M., Xue, M., Morrison, H., Milbrandt, J., Korolev, A.V., Hu, Y., Qu, Z., Wolde, M., Nguyen, C., Schwarzenboeck, A., Heckman, I., 2022. Microphysical processes producing high ice water contents (HIWCs) in tropical convective clouds during the HAIC-HIWC field campaign: dominant role of secondary ice production. Atmospheric Chem. Phys. 22, 2365–2384. https://doi.org/10.5194/acp-22-2365-2022

Hudson, J.G., Yum, S.S., 2001. Maritime–continental drizzle contrasts in small cumuli. J. Atmospheric Sci. 58, 915–926.

Kessler, E., 1969. On the distribution and continuity of water substance in atmospheric circulations, in: On the Distribution and Continuity of Water Substance in Atmospheric Circulations. Springer, pp. 1–84.

Klein, S.A., Hartmann, D.L., 1993. The seasonal cycle of low stratiform clouds. J. Clim. 6, 1587–1606.

Korolev, A., Heckman, I., Wolde, M., Ackerman, A.S., Fridlind, A.M., Ladino, L.A., Lawson, R.P., Milbrandt, J., Williams, E., 2020. A new look at the environmental conditions favorable to

secondary ice production. Atmospheric Chem. Phys. 20, 1391–1429.
Lac, C., Chaboureau, P., Masson, V., Pinty, P., Tulet, P., Escobar, J., Leriche, M., Barthe, C., Aouizerats, B., Augros, C., others, 2018. Overview of the Meso-NH model version 5.4 and its applications. Geosci. Model Dev. 11, 1929–1969.
Lawson, R.P., Angus, L.J., Heymsfield, A.J., 1998. Cloud particle measurements in thunderstorm anvils and possible weather threat to aviation. J. Aircr. 35, 113–121.
Lebeaupin Brossier, C., 2007. Étude du couplage océan-atmosphère associé aux épisodes de pluie intense en région méditérannéenne (PhD Thesis). Toulouse 3.
Lellouche, J.-M., Greiner, E., Le Galloudec, O., Garric, G., Regnier, C., Drevillon, M., Benkiran, M., Testut, C.-E., Bourdalle-Badie, R., Gasparin, F., others, 2018. Recent updates to the Copernicus Marine Service global ocean monitoring and forecasting real-time 1/ 12° high-resolution system. Ocean Sci. 14, 1093–1126.
Leroy, D., Fontaine, E., Schwarzenboeck, A., Strapp, J.W., Korolev, A., McFarquhar, G., Dupuy, R., Gourbeyre, C., Lilie, L., Protat, A., others, 2017. Ice crystal sizes in high ice water content clouds. Part II: Statistics of mass diameter percentiles in tropical convection observed during the HAIC/HIWC project. J. Atmospheric Ocean. Technol. 34, 117–136.
Lo, K.K., Passarelli, R.E., 1982. The growth of snow in winter storms:. An airborne observational study. J. Atmospheric Sci. 39, 697–706.
Lo, K.-W.K., 1983. Growth processes of snow (PhD Thesis). Massachusetts Institute of Technology.
Locatelli, J.D., Hobbs, P.V., 1974. Fall speeds and masses of solid precipitation particles. J. Geophys. Res. 79, 2185–2197.
Lord, S.J., Willoughby, H.E., Piotrowicz, J.M., 1984. Role of a Parameterized Ice-Phase Microphysics in an Axisymmetric, Nonhydrostatic Tropical Cyclone Model. J. Atmospheric Sci. 41, 2836–2848. https://doi.org/10.1175/1520-0469(1984)041<2836:ROAPIP>2.0.CO;2
Marshall, J.S., Palmer, W.M.K., 1948. The distribution of raindrops with size. J. Meteorol. 5, 165–166.
Mason, J., Strapp, W., Chow, P., 2006. The ice particle threat to engines in flight, in: 44th AIAA Aerospace Sciences Meeting and Exhibit. p. 206.
Mason, J.G., Grzych, M., 2011. The challenges identifying weather associated with jet engine ice crystal icing. SAE Technical Paper.
Masson, V., Le Moigne, P., Martin, E., Faroux, S., Alias, A., Alkama, R., Belamari, S., Barbu, A., Boone, A., Bouyssel, F., Brousseau, P., Brun, E., Calvet, J.-C., Carrer, D., Decharme, B., Delire, C., Donier, S., Essaouini, K., Gibelin, A.-L., Giordani, H., Habets, F., Jidane, M., Kerdraon, G., Kourzeneva, E., Lafaysse, M., Lafont, S., Lebeaupin Brossier, C., Lemonsu, A., Mahfouf, J.-F., Marguinaud, P., Mokhtari, M., Morin, S., Pigeon, G., Salgado, R., Seity, Y., Taillefer, F., Tanguy, G., Tulet, P., Vincendon, B., Vionnet, V., Voldoire, A., 2013. The SURFEXv7.2 land and ocean surface platform for coupled or offline simulation of Earth surface variables and fluxes. Geosci. Model Dev. 6, 929–960. https://doi.org/10.5194/gmd-6-929-2013
Meyers, M.P., DeMott, P.J., Cotton, W.R., 1992. New primary ice-nucleation parameterizations in an explicit cloud model. J. Appl. Meteorol. 31, 708–721.
Mitchell, D.L., 1991. Evolution of snow-size spectra in cyclonic storms. Part II: Deviations from the exponential form. J. Atmospheric Sci. 48, 1885–1899.
Mitchell, D.L., 1988. Evolution of snow-size spectra in cyclonic storms. Part I: Snow growth by vapor deposition and aggregation. J. Atmospheric Sci. 45, 3431–3451.
Mlawer, E.J., Taubman, S.J., Brown, P.D., Iacono, M.J., Clough, S.A., 1997. Radiative transfer for inhomogeneous atmospheres: RRTM, a validated correlated-k model for the longwave. J. Geophys. Res. Atmospheres 102, 16663–16682.
Morcrette, J.-J., 1991. Radiation and cloud radiative properties in the European Centre for Medium Range Weather Forecasts forecasting system. J. Geophys. Res. Atmospheres 96, 9121–9132. https://doi.org/10.1029/89JD01597

Morrison, H., Milbrandt, J.A., 2015. Parameterization of cloud microphysics based on the prediction of bulk ice particle properties. Part I: Scheme description and idealized tests. J. Atmospheric Sci. 72, 287–311.

Morrison, H., Thompson, G., Tatarskii, V., 2009. Impact of cloud microphysics on the development of trailing stratiform precipitation in a simulated squall line: Comparison of one-and two-moment schemes. Mon. Weather Rev. 137, 991–1007.

Passarelli, R.E., 1978. An approximate analytical model of the vapor deposition and aggregation growth of snowflakes. J. Atmospheric Sci. 35, 118–124.

Pergaud, J., Masson, V., Malardel, S., Couvreux, F., 2009. A parameterization of dry thermals and shallow cumuli for mesoscale numerical weather prediction. Bound.-Layer Meteorol. 132, 83.

Pinty, J.-P., Jabouille, P., 1998. A mixed-phase cloud parameterization for use in mesoscale non-hydrostatic model: simulations of a squall line and of orographic precipitations, in: Conf. on Cloud Physics. Amer. Meteor. Soc Everett, WA, pp. 217–220.

Proctor, F., Harrah, S., Switzer, G.F., Strickland, J.K., Hunt, P.J., 2017. High ice water concentrations in the 19 August 2015 coastal mesoconvective system, in: 9th AIAA Atmospheric and Space Environments Conference. p. 4370.

Riette, S., 2020. Development of “Physical Parametrizations with PYthon”(PPPY, version 1.1) and its usage to reduce the time-step dependency in a microphysical scheme. Geosci. Model Dev. 13, 443–460.

Ryan, B.F., 2000. A bulk parameterization of the ice particle size distribution and the optical properties in ice clouds. J. Atmospheric Sci. 57, 1436–1451.

Schaefer, V.S., 1962. Condensed Water in the Free Atmosphere in Air Colder than- 40C. J. Appl. Meteorol. 1, 481–488.

Seity, Y., Brousseau, P., Malardel, S., Hello, G., Bénard, P., Bouttier, F., Lac, C., Masson, V., 2011. The AROME-France convective-scale operational model. Mon. Weather Rev. 139, 976–991.

Tao, W.-K., Simpson, J., McCumber, M., 1989. An Ice-Water Saturation Adjustment. Mon. Weather Rev. 117, 231–235. https://doi.org/10.1175/1520-0493(1989)117<0231:AIWSA>2.0.CO;2

Thompson, G., Field, P.R., Rasmussen, R.M., Hall, W.D., 2008. Explicit forecasts of winter precipitation using an improved bulk microphysics scheme. Part II: Implementation of a new snow parameterization. Mon. Weather Rev. 136, 5095–5115.

Vié, B., Pinty, J.-P., Berthet, S., Leriche, M., 2016. LIMA (v1. 0): A quasi two-moment microphysical scheme driven by a multimodal population of cloud condensation and ice freezing nuclei. Geosci. Model Dev. 9, 567–586.

Wall, C.J., Norris, J.R., Gasparini, B., Smith Jr, W.L., Thieman, M.M., Sourdeval, O., 2020. Observational Evidence that Radiative Heating Modifies the Life Cycle of Tropical Anvil Clouds. J. Clim. 33, 8621–8640.

Walters, D., Boutle, I., Brooks, M., Melvin, T., Stratton, R., Vosper, S., Wells, H., Williams, K., Wood, N., Allen, T., 2017. The Met Office unified model global atmosphere 6.0/6.1 and JULES global land 6.0/6.1 configurations. Geosci. Model Dev. 10, 1487–1520.

Wurtz, J., Bouniol, D., Vié, B., Lac, C., 2021. Evaluation of the AROME model’s ability to represent ice crystal icing using in situ observations from the HAIC 2015 field campaign. Q. J. R. Meteorol. Soc. n/a. https://doi.org/10.1002/qj.4100

# Tables

| | Graupel | Pristine ice (plates) | Snow | Rain | Liquid cloud water |
|---|---|---|---|---|---|
| **a** | 19,6 | 0,82 | 0,02 | 524 | 524 |
| **b** | 2.8 | 2.5 | 1.9 | 3 | 3 |
| **c** | 124 | 800 | 5.1 | 842 | $3.2x10^7$ |
| **d** | 0.66 | 1 | 0.27 | 0.8 | 2 |
| **α** | 1 | 3 | 1 | 1 | 3 (ocean)<br>1 (continent) |
| **ν** | 1 | 3 | 1 | 1 | 1 (ocean)<br>3 (continent) |
| **C** | 1E5 | X | 5 | 8E6 | X |
| **x** | -0.5 | X | 1 | -1 | X |

*Table I: Coefficient values (S.I. unit), describing the ICE3 ice species*

487

| | c | d | f |
|---|---|---|---|
| L&H –large aggregates (2000μm to 12000μm) | 5.1 | 0.27 | 0 |
| L&H – small aggregates (200μm to 3000μm) | 11.72 | 0.41 | 0 |
| Extended L&H – Marshall-Palmer | 13.2 | 0.423 | 25.14 |
| Extended L&H – Generalized Gamma (α=0.214) | 11.52 | 0.39 | 0.097 |

*Table II: Values of (c, d, f) triplets of the terminal fall speed – diameter law*

| Experiment name | λ parameterization | PSD shape | Terminal fall speed |
|---|---|---|---|
| OPER | $N_t = C\lambda^x$ (Caniaux, 1993) | Marshall-Palmer | L&H (large) |
| HAIC-MP | $\lambda(T)$ from the HAIC dataset | Marshall-Palmer | L&H (large) |
| HOUZE-MP | $\lambda(T)$ from (Houze et al., 1979) dataset | Marshall-Palmer | L&H (large) |
| HAIC-GG | $\lambda(T)$ from the HAIC dataset | Generalized Gamma | L&H (large) |
| Vt | $N_t = C\lambda^x$ (Caniaux, 1993) | Marshall-Palmer | Extended L&H |
| HAIC-MP-Vt | $\lambda(T)$ from the HAIC dataset | Marshall-Palmer | Extended L&H |
| HAIC-GG-Vt | $\lambda(T)$ from the HAIC dataset | Generalized Gamma | Extended L&H |

*Table III: Sum-up of all experiments.*

| Experiment name | Convective | Stratiform | Cirriform |
|---|---|---|---|
| Vt | +8% | -4% | -21% |
| HAIC-MP | -8% | +29% | +27% |
| HOUZE-MP | -7% | +26% | +28% |
| HAIC-GG | -7% | +28% | +30% |
| HAIC-MP-Vt | -6% | +37% | +57% |
| HAIC-GG-Vt | -6% | +42% | +69% |

*Table IV: Area difference in percentage of each sub-region compared to the OPER simulation.*

# Figures

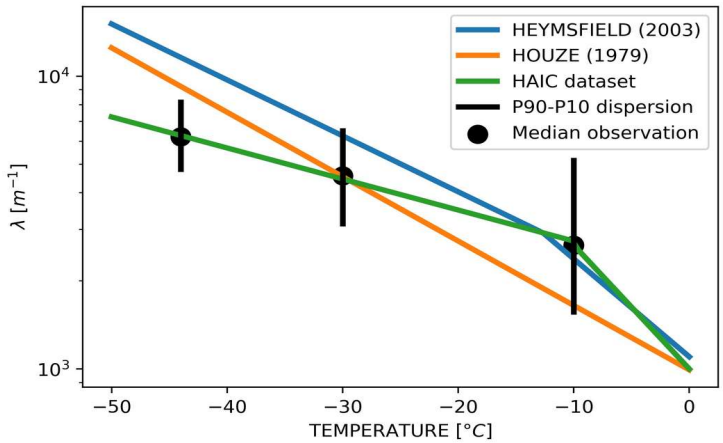


*Figure 1: Parameterization of λ following Houze et al. (1979) (orange), Heymsfield et al. (2003) (blue) and as derived from the HAIC 2015 dataset .*

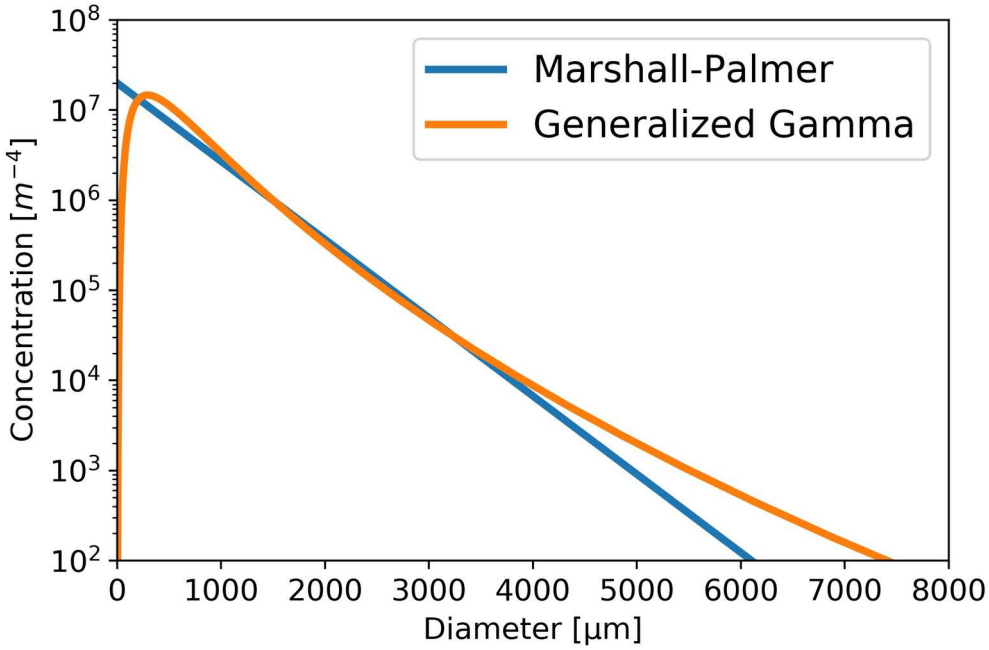


*Figure 2: Comparison of the Marshall-Palmer and the generalized gamma shape (α= 0.214 and ν=43.7) for $N_t = 10^4\ m^{-3}$ and $\lambda=2000 m^{-1}$. Equivalent λ is used for the generalized gamma shape.*

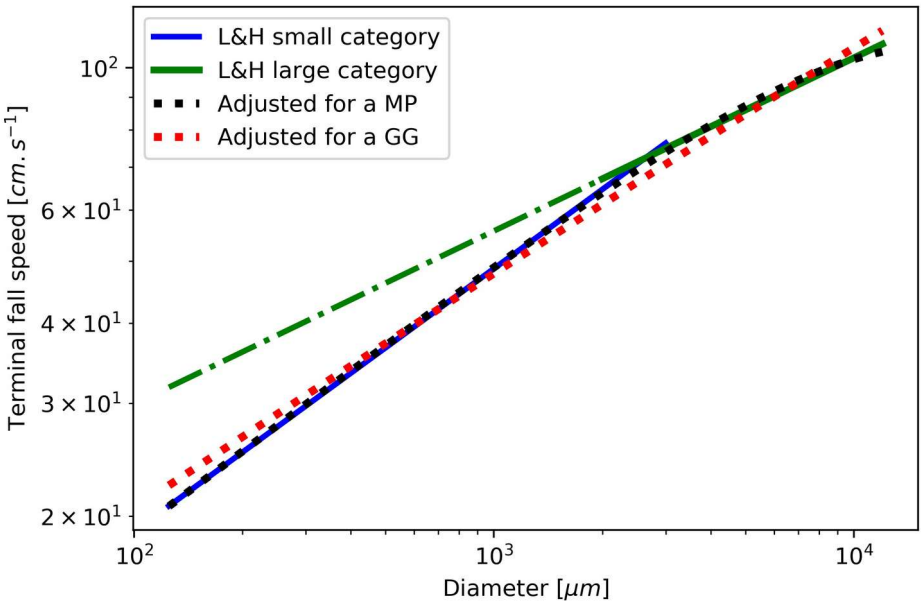


*Figure 3: Terminal fall speed of snow as a function of its diameter computed for a air density of 0.5 kg.m$^{-3}$. Blue and green lines show the Locatelli & Hobbs (1974) measurement fits for respectively small (<3000µm) and big snow (>2000µm) particles and dash-dotted line shows the law outside of its range of validity.*

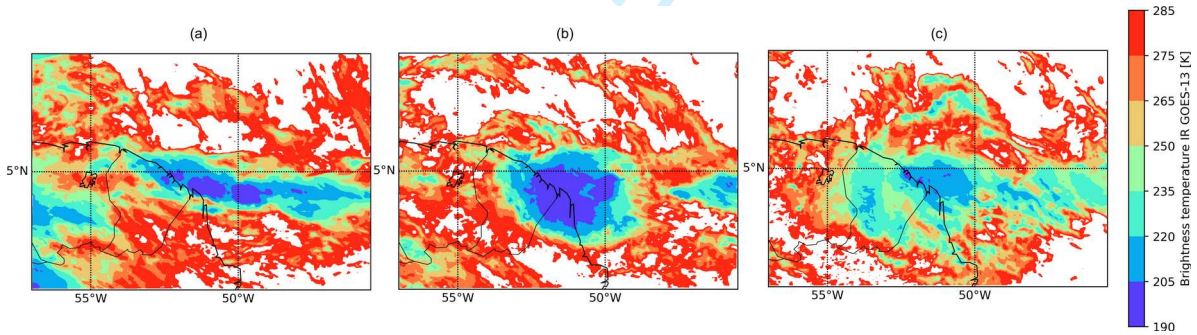


*Figure 4: Infra-red brightness temperature retrieved by GOES-13 in the case of the 29 May 2015 near French Guiana at 05UTC15 (a), 9UTC45 (b) and 14UTC45 (c).*

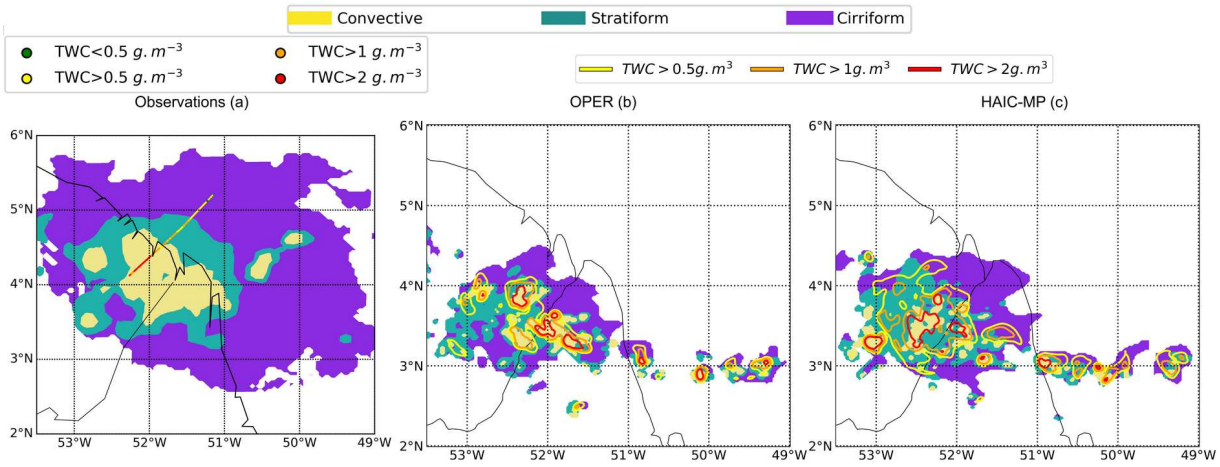


*Figure 5: Cloud organization of case study at 10UTC as sampled by satellite observations and as simulated in AROME OPER (b) and HAIC-MP (c). Filled contours indicate the sub-region of these MCSs : yellow represents convective regions, green represents stratiform regions and purple represents cirriform regions. TWC sampled at -30°C by during the HAIC field campaign is indicated by dots in (a) and TWC simulated at -30°C by AROME simulations (b and c) by contours.*

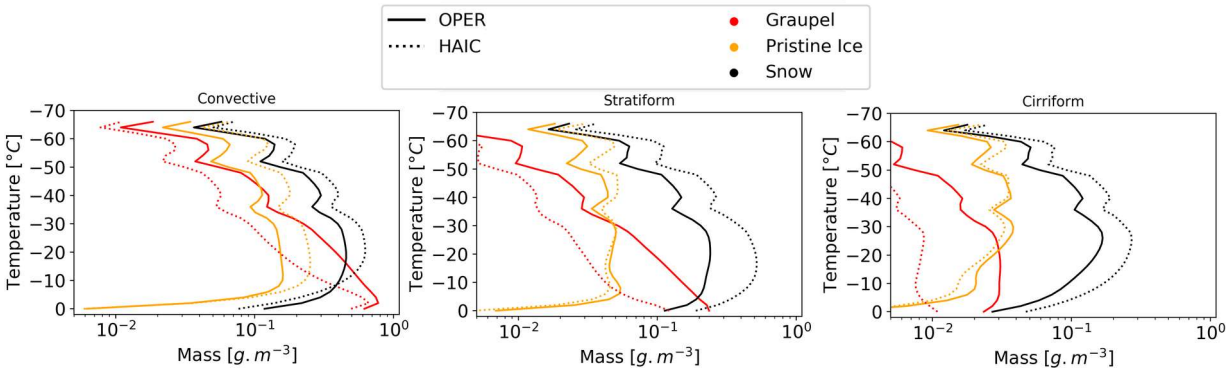


*Figure 6: Vertical mean of microphysical composition in the convective (a) , stratiform (b) and cirriform (c) region of MCS.*

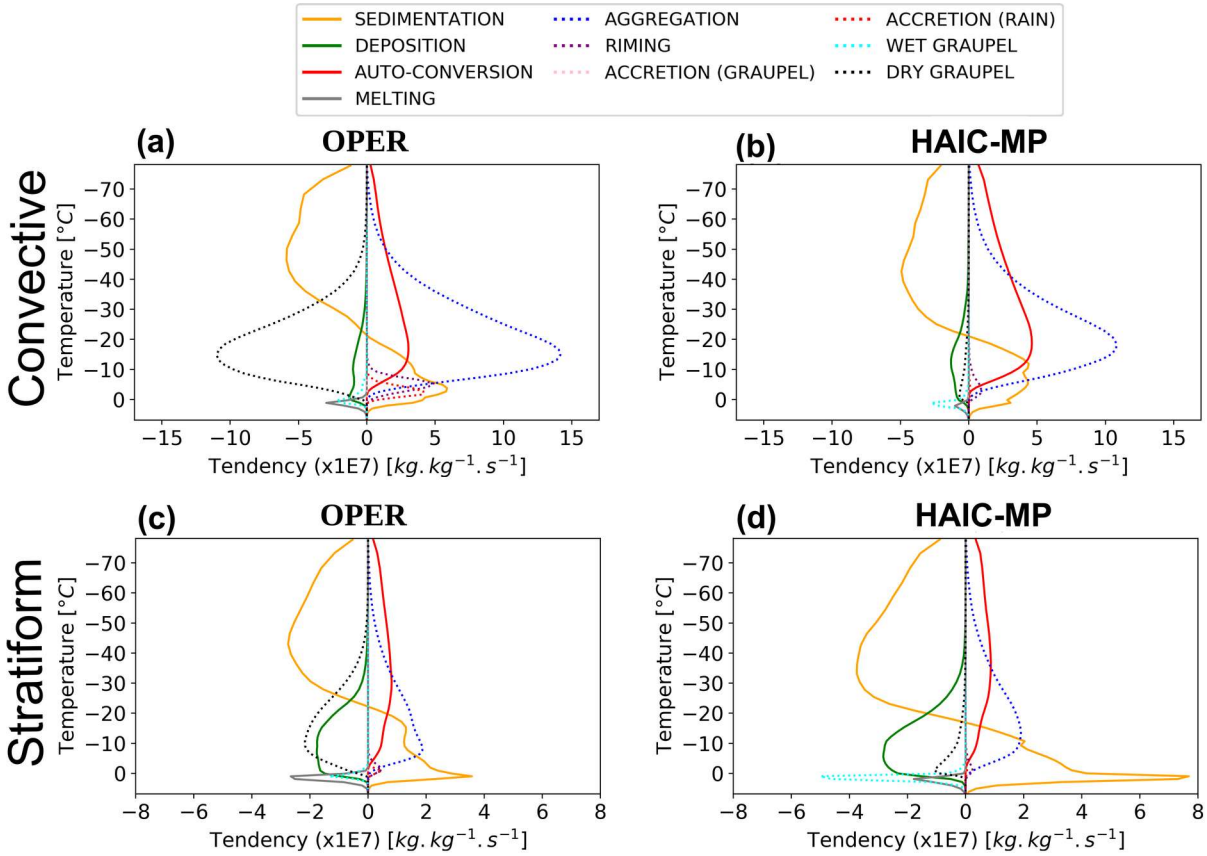


*Figure 7: Mean snow mass tendencies for each process involving snow in convective (upper part) and stratiform (lower part) regions. the left panel (a and c) are for the OPER experiment while the right panel (b and d) are for HAIC-MP. Tendencies are multiplied by $10^7$. Non-collection is represented by solid lines. The orange curve is for sedimentation, the green one is for deposition, the red one is for auto-conversion of pristine ice,the gray one is for the melting of snow. Dotted lines represent collection processes. The blue curve is for aggregation, the purple one represents riming, the pink one accretion of graupel, the red one accretion of rain, the cyan purple one for riming, the pink one for the accretion of graupel, the red one for accretion of rain and finally, the cyan and black curves represent graupel growth in respectively wet and dry modes.*

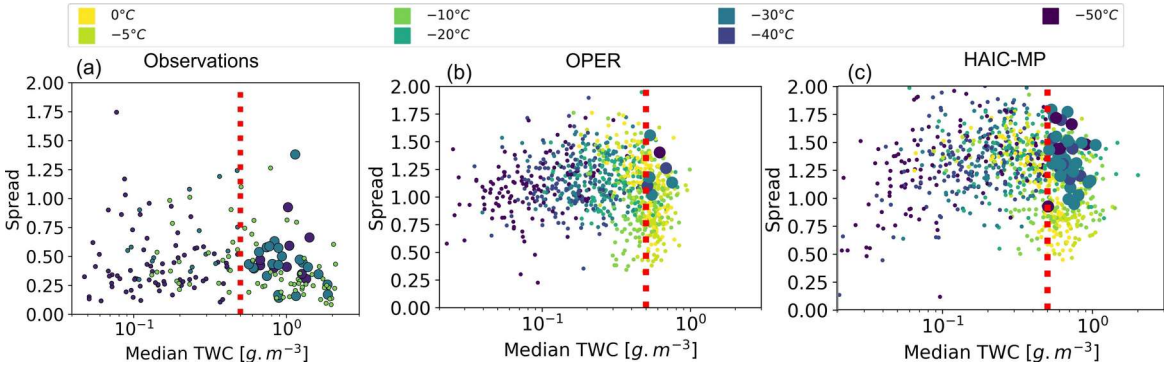


*Figure 8: Scatter plots of TWC Spread and median value within each stratiform sampled segment (a) or within each simulated stratiform region (b and c). Colors show the sampling temperature.*

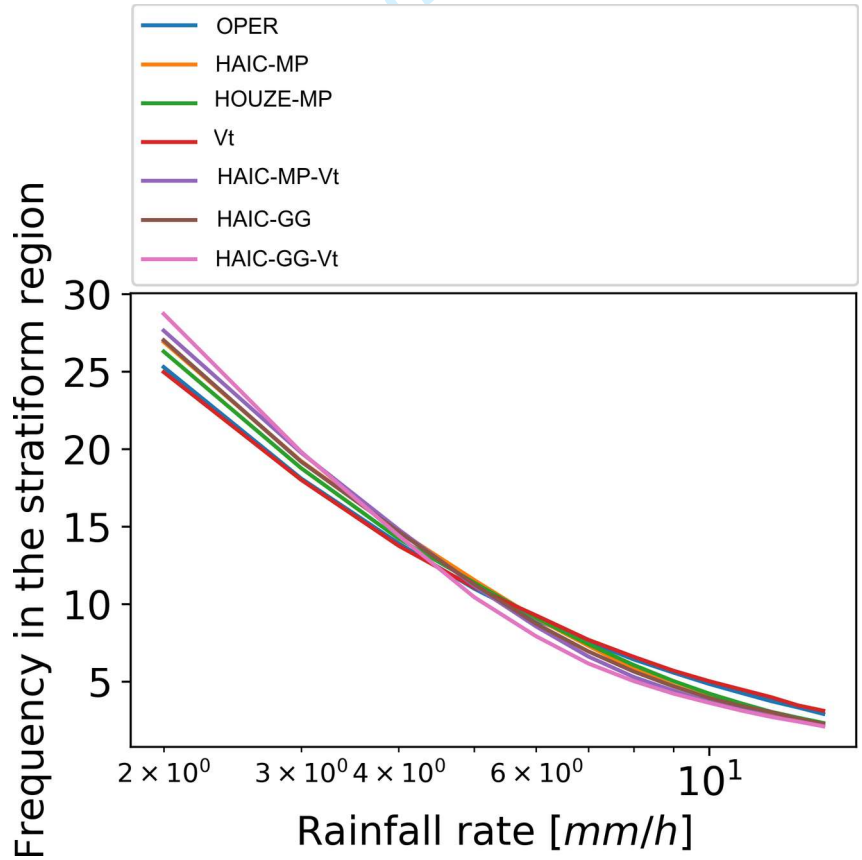


*Figure 9: Rainfall rate distribution in the stratiform region.*

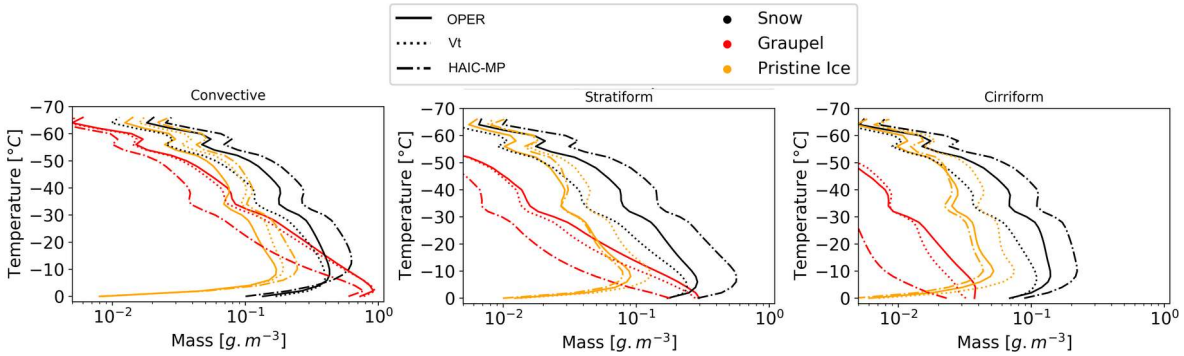


*Figure 10: Vertical mean of microphysical composition in the convective (a) , stratiform (b) and cirriform (c) region of MCS.*

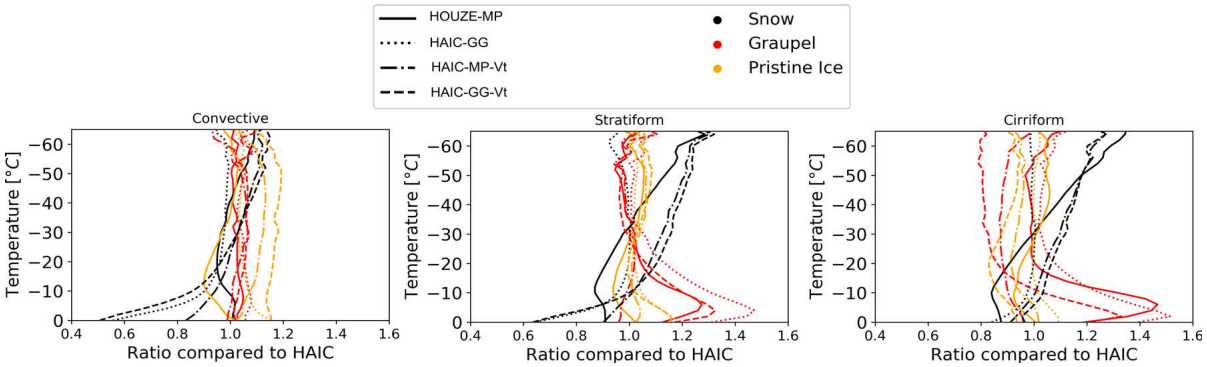


*Figure 11: Vertical mean profile of ice hydrometeors for HOUZE-MP (straight), HAIC-GG (dotted), HAIC-MP-Vt (dash-dotted) and HAIC-GG-Vt (dashed) compared to the HAIC experiment in the convective (a), stratiform (b) and cirriform (c) regions.*

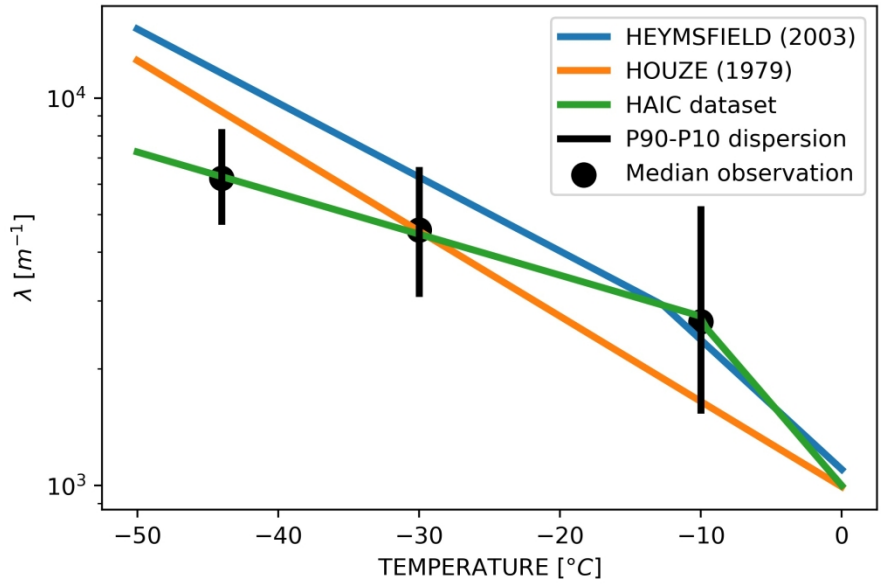


Parameterization of λ following Houze et al. (1979) (orange), Heymsfield et al. (2003) (blue) and as derived from the HAIC 2015 dataset (Wurtz et al. 2021).

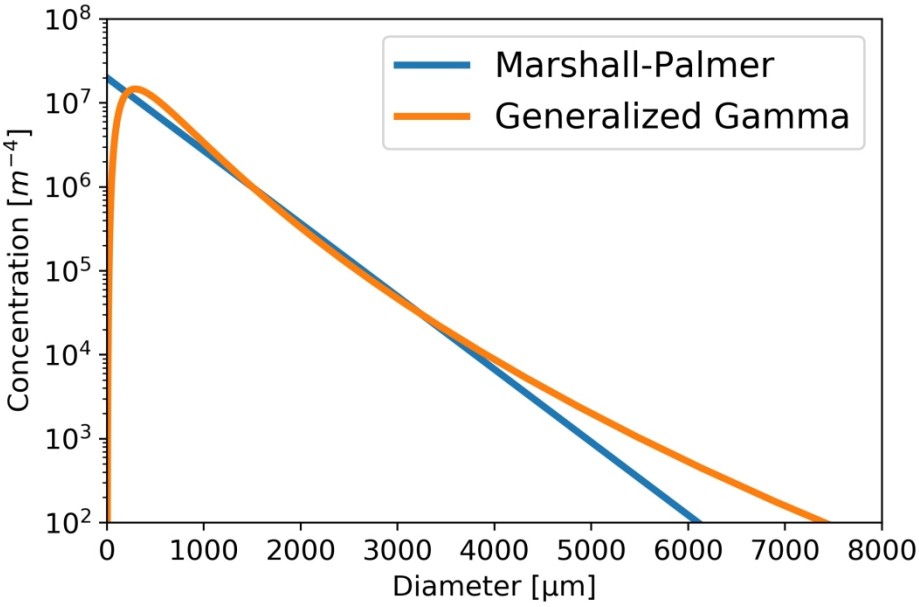


Comparison of the Marshall-Palmer and the generalized gamma shape (α= 0.214 and ν=43.7) for Nt = 104 m-3 and λ=2000m-1. Equivalent λ is used for the generalized gamma shape.

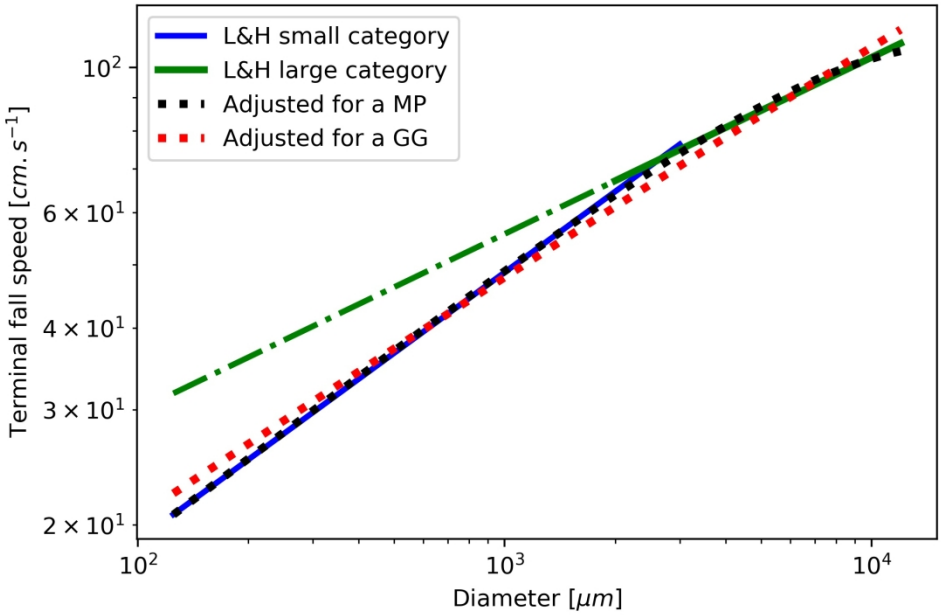


Terminal fall speed of snow as a function of its diameter computed for a air density of 0.5 kg.m-3. Blue and green lines show the Locatelli & Hobbs (1974) measurement fits for respectively small (<3000µm) and big snow (>2000µm) particles and dash-dotted line shows the law outside of its range of validity.

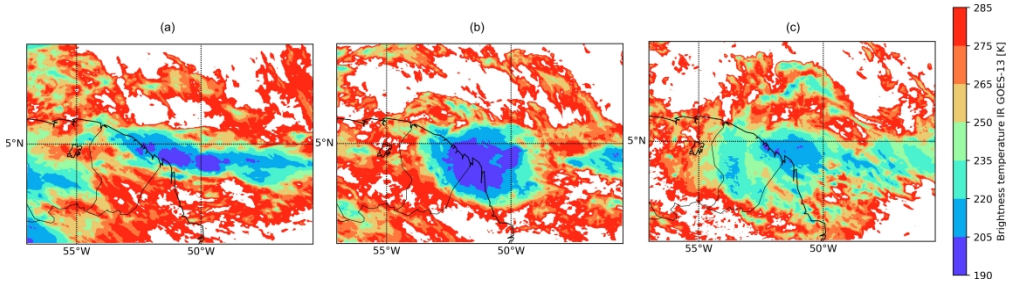


Infra-red brightness temperature retrieved by GOES-13 in the case of the 29 May 2015 near French Guiana at 05UTC15 (a), 9UTC45 (b) and 14UTC45 (c).

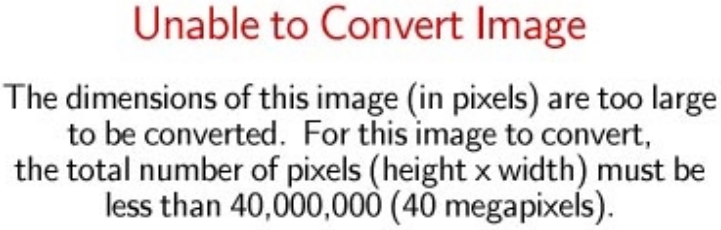


Cloud organization of case study at 10UTC as sampled by satellite observations and as simulated in AROME OPER (b) and HAIC-MP (c). Filled contours indicate the sub-region of these MCSs : yellow represents convective regions, green represents stratiform regions and purple represents cirriform regions. TWC sampled at -30°C by during the HAIC field campaign is indicated by dots in (a) and TWC simulated at -30°C by AROME simulations (b and c) by contours.

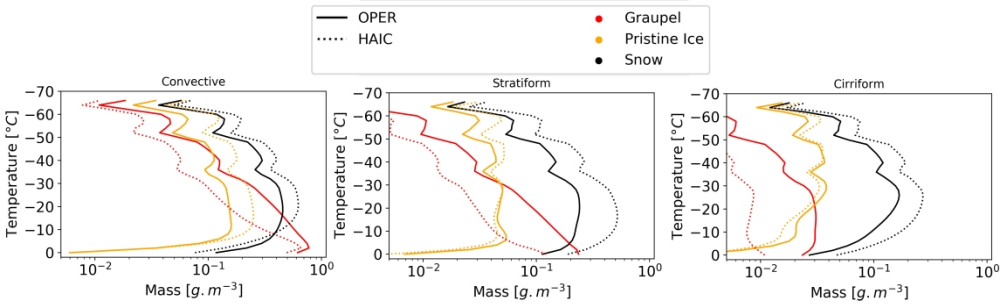


Vertical mean of microphysical composition in the convective (a) , stratiform (b) and cirriform (c) region of MCS.

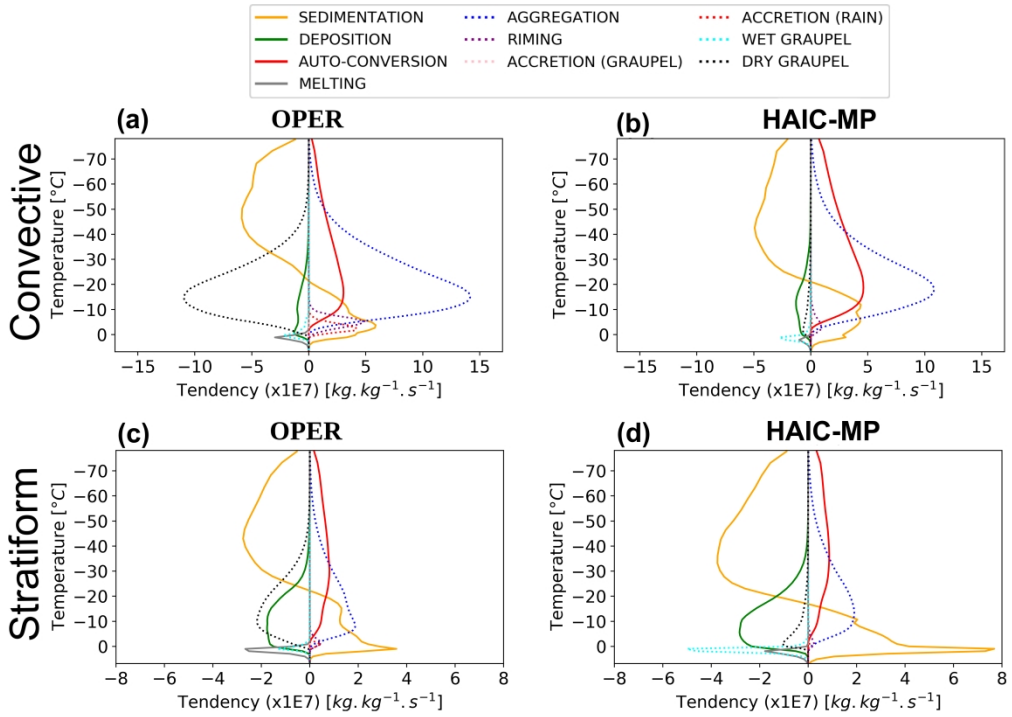


Mean snow mass tendencies for each process involving snow in convective (upper part) and stratiform (lower part) regions. the left panel (a and c) are for the OPER experiment while the right panel (b and d) are for HAIC-MP. Tendencies are multiplied by 107. Non-collection is represented by solid lines. The orange curve is for sedimentation, the green one is for deposition, the red one is for auto-conversion of pristine ice,the gray one is for the melting of snow. Dotted lines represent collection processes. The blue curve is for aggregation, the purple one represents riming, the pink one accretion of graupel, the red one accretion of rain, the cyan purple one for riming, the pink one for the accretion of graupel, the red one for accretion of rain and finally, the cyan and black curves represent graupel growth in respectively wet and dry modes.

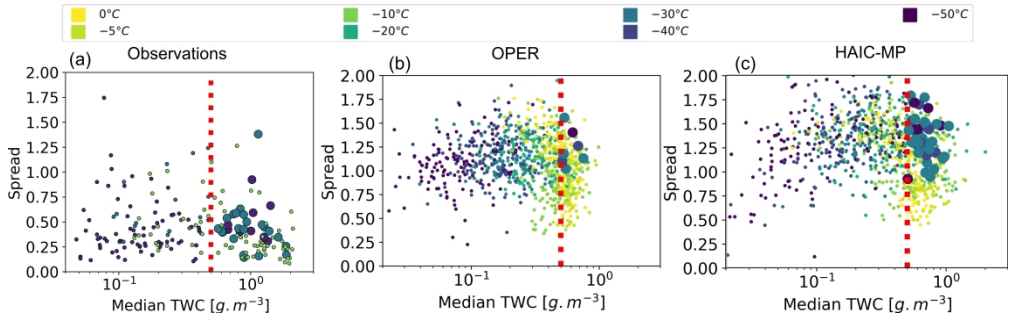


Scatter plots of TWC Spread and median value within each stratiform sampled segment (a) or within each simulated stratiform region (b and c). Colors show the sampling temperature.

2091x645mm (72 x 72 DPI)

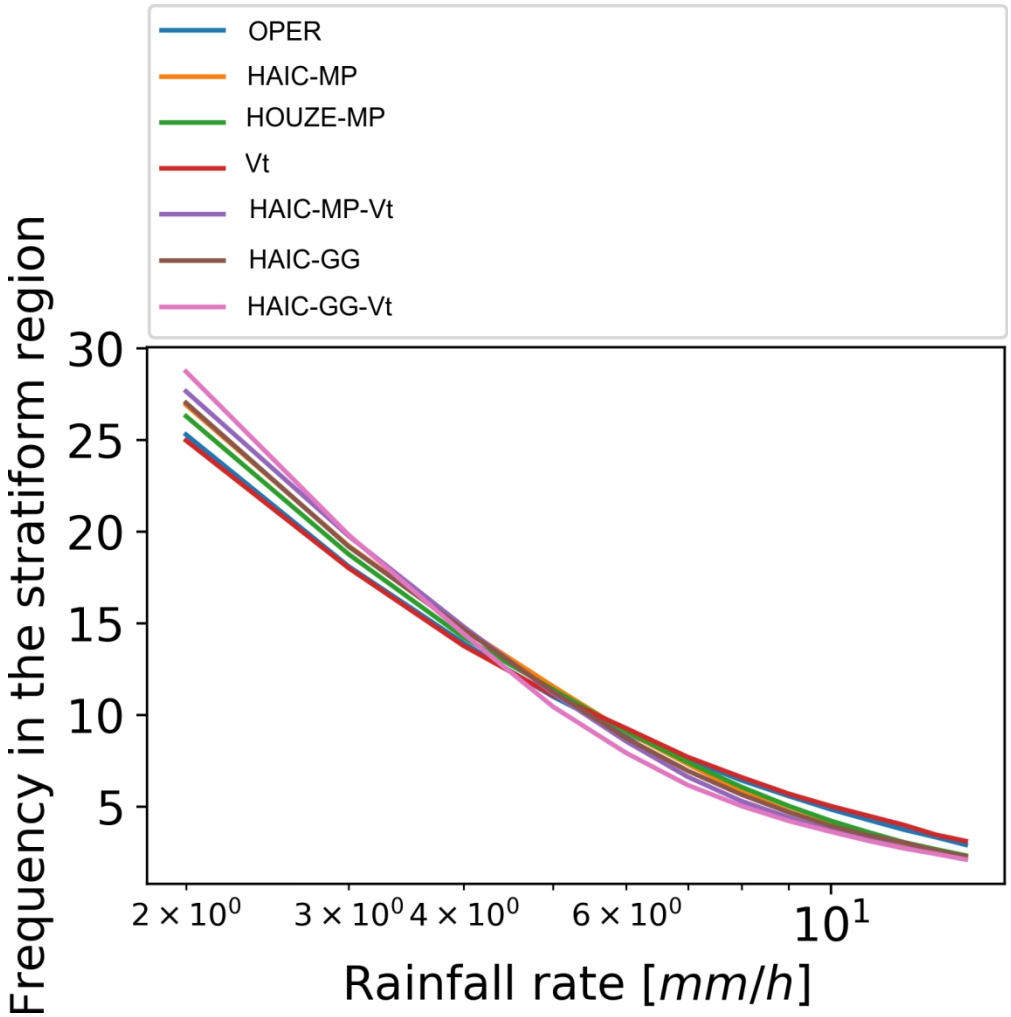


Rainfall rate distribution in the stratiform region.

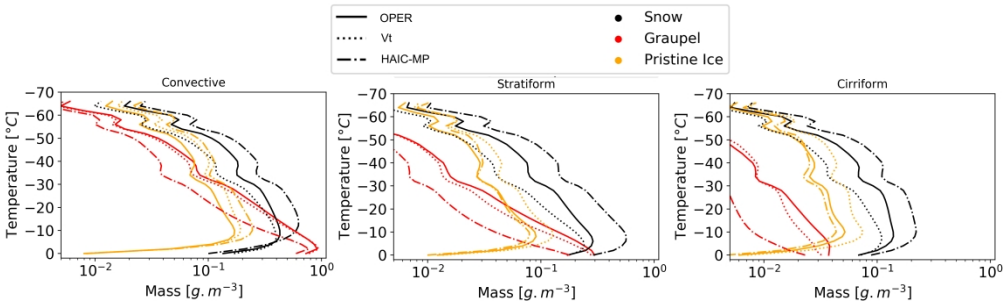


Vertical mean of microphysical composition in the convective (a) , stratiform (b) and cirriform (c) region of MCS.

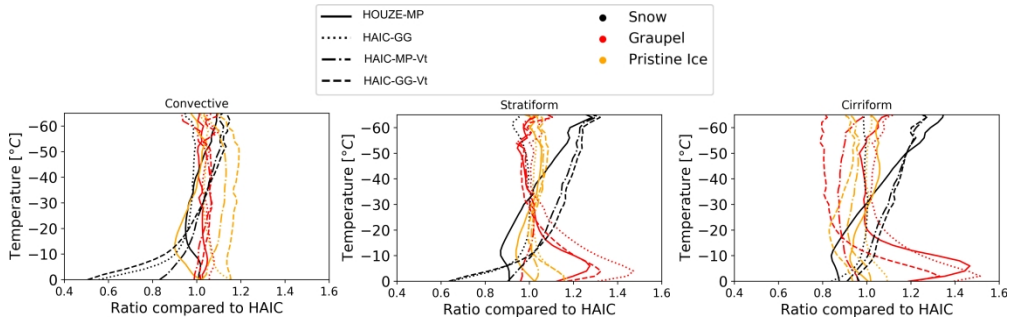


Vertical mean profile of ice hydrometeors for HOUZE-MP (straight), HAIC-GG (dotted), HAIC-MP-Vt (dash-dotted) and HAIC-GG-Vt (dashed) compared to the HAIC experiment in the convective (a), stratiform (b) and cirriform (c) regions.

| | Graupel | Pristine ice (plates) | Snow | Rain | Liquid cloud water |
|---|---|---|---|---|---|
| **a** | 19,6 | 0,82 | 0,02 | 524 | 524 |
| **b** | 2.8 | 2.5 | 1.9 | 3 | 3 |
| **c** | 124 | 800 | 5.1 | 842 | $3.2 \times 10^7$ |
| **d** | 0.66 | 1 | 0.27 | 0.8 | 2 |
| **α** | 1 | 3 | 1 | 1 | 3 (ocean)<br>1 (continent) |
| **ν** | 1 | 3 | 1 | 1 | 1 (ocean)<br>3 (continent) |
| **C** | 1E5 | X | 5 | 8E6 | X |
| **x** | -0.5 | X | 1 | -1 | X |

*Table 1: Coefficient values (S.I. unit), describing the ICE3 ice species*

| | c | d | f |
|---|---|---|---|
| L&H –large aggregates (2000µm to 12000µm) | 5.1 | 0.27 | 0 |
| L&H – small aggregates (200µm to 3000µm) | 11.72 | 0.41 | 0 |
| Extended L&H – Marshall-Palmer | 13.2 | 0.423 | 25.14 |
| Extended L&H – Generalized Gamma (α=0.214) | 11.52 | 0.39 | 0.097 |

*Table 1: Values of (c, d, f) triplets of the terminal fall speed – diameter law*

| Experiment name | λ parameterization | PSD shape | Terminal fall speed |
|---|---|---|---|
| OPER | $N_t = C\lambda^x$ (Caniaux, 1993) | Marshall-Palmer | L&H (large) |
| HAIC-MP | $\lambda(T)$ from the HAIC dataset | Marshall-Palmer | L&H (large) |
| HOUZE-MP | $\lambda(T)$ from Houze et al. (1979) dataset | Marshall-Palmer | L&H (large) |
| HAIC-GG | $\lambda(T)$ from the HAIC dataset | Generalized Gamma | L&H (large) |
| Vt | $N_t = C\lambda^x$ (Caniaux, 1993) | Marshall-Palmer | Extended L&H |
| HAIC-MP-Vt | $\lambda(T)$ from the HAIC dataset | Marshall-Palmer | Extended L&H |
| HAIC-GG-Vt | $\lambda(T)$ from the HAIC dataset | Generalized Gamma | Extended L&H |

| Experiment name | Convective | Stratiform | Cirriform |
|---|---|---|---|
| Vt | +8% | -4% | -21% |
| HAIC-MP | -8% | +29% | +27% |
| HOUZE-MP | -7% | +26% | +28% |
| HAIC-GG | -7% | +28% | +30% |
| HAIC-MP-Vt | -6% | +37% | +57% |
| HAIC-GG-Vt | -6% | +42% | +69% |

# ***Improvements to the parameterization of snow in AROME in the context of ice crystal icing***

*Jean Wurtz*, Dominique Bouniol, Benoît Vié*

*CNRM, Université de Toulouse, Météo-France, CNRS, Toulouse, France*

*Corresponding author: Jean Wurtz, CNRM - Météo-France, 42 avenue Gaspard Coriolis, 31057 Toulouse, France. email: jean.wurtz@meteo.fr*

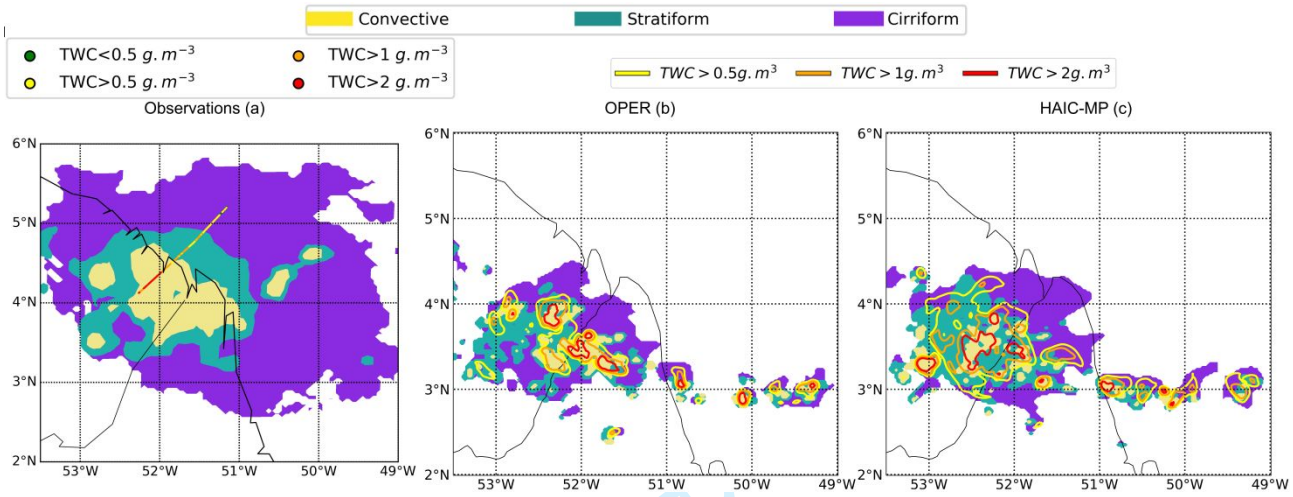


Ice crystal icing (ICI) poses a threat nowadays for airplane pilots crossing the anvil of tropical meso-scale convective systems (MCS). In this article, the capability

to forecast such weather conditions using mesoscale French forecast system AROME is enhanced and broad stratiform areas with sustained and high ice water is made possible. To do so, the one-moment microphysics of AROME (ICE3) and its representation of snow species has been modified.